Test Beam Analysis for HGTD Sensors

Adrián Vásquez (USB)
Supervisors: **Giulia Di Gregorio (CERN), Stefano Manzoni (CERN)**

August 23, 2024

Abstract

For the high luminosity upgrade of the LHC at CERN, ATLAS is considering the addition of a High Granularity Timing Detector (HGTD) in front of the end cap and forward calorimeters at $|z| = 3.5m$ and covering the region $2.4 < \eta < 4$ to help to reduce the effect of pile-up. The chosen sensors are arrays of Low Gain Avalanche Detectors (LGAD). This project aimed to the characterization of 8 LGAD sensors based on Test Beam campaign performed in May 2024 at CERN SPS. The time resolution and collected charge for the 8 sensors are provided.

Contents

1 Introduction

The Large Hadron Collider (or LHC) is the largest and most powerful particle accelerator in the world. It is located 175 meters underground at CERN, near Geneva [1]. It consists of a 27 kilometre long ring formed by cavities that increase the energy of the particles inside and consequently accelerate them. From here, the proton halos inside the LHC collide at four locations around the ring, which correspond to the position of four particle detectors: ATLAS, CMS, ALICE and LHCb [1].

Now, with respect to the four detectors just mentioned, ATLAS will be of special interest. ATLAS (A Toroidal Apparatus of the LHC) is a general-purpose experiment, which includes the study of the Standard Model, measurements of the properties of the Higgs boson, and research into new physics such as supersymmetry and dark matter. This detector was designed to provide accurate reconstruction of muons, photons, electrons, tau leptons, jets, and lost transverse energy under high luminosity conditions [1, 3].

Having this clear, an important indicator of the performance of an accelerator is its luminosity, which is proportional to the number of collisions that occur in a given time [6]. The expression for luminosity ($\mathcal{L}$) is given by:

$$\mathcal{L} = \frac{1}{\sigma}\frac{dN}{dt}[cm^{-2}s^{-1}] \tag{1}$$

where σ corresponds to the cross section, N is the number of potential collisions and t is the time.

The higher the luminosity, the greater the amount of data that experiments can collect and, consequently, the greater the probability of observing rare processes. This is where the project known as the *High Luminosity Large Hadron Collider* (HL-LHC) comes into play. Its goal is to improve the performance of the LHC to increase the potential for discoveries. The goal is to increase the integrated luminosity by a factor greater than 10 over the LHC design value [3].

(HL-LHC) is planned to begin colliding protons in 2028. This accelerator upgrade will also induce a higher number of collisions per intersection (around 200). This phenomenon is called Pile-up (μ), and to address this increase in collisions, ATLAS is preparing a complex series of updates that include the installation of new subdetectors [6].

Among these new ATLAS upgrades, there's one of special interest characterized by the installation of a subdetector called the High Granularity timming Detector or HGTD. The HGTD will allow a significant improvement in ATLAS performance by providing better separation between events resulting from intense scattering and those related to *Pile-up*. The *Pile-up* is a phenomenon characterized by an abrupt increase in the number of collisions per bunch of particles that cross a certain area, which occurs as a result of the increase in luminosity and, therefore, is one of the main challenges to overcome due to the new updates ATLAS is experiencing. In figure 1 a graphic example of *Pile-Up* can be seen, where it is observed that by increasing the aforementioned number of collisions from 25 to 250 the number of tracks of the resulting particles abruptly increases.

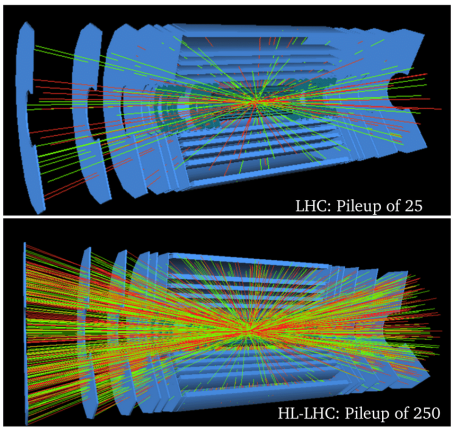

Figure 1: *Pile-Up* representation before and after the HL-LHC

Due to the high radiation levels expected in this region for an integrated luminosity of $L = 4000 fb^{-1}$, the detector sensors and front-end electronics must sustain a 1 MeV neutron equivalent fluence of up to 3.7×10^{15} neutrons/cm^2 and 4.5 MGy total ionising dose (at R=120 mm, including a safety factor of 1.5 and assuming one replacement of the inner part after half of the lifetime), while providing the challenging time resolution requirements of approximately 30 ps per minimum ionising particle (MIP). The sensor choice for the HGTD, given the need for accurate time measurement, are Low Gain Avalanche Detector (LGAD) pads with a thickness of about $50\mu m$ and a pad area of $1.3 \times 1.3mm^2$ [1].

The time resolution of the sensor is given by the quadratic sum of the dispersion due to non-uniform energy deposition along the sensor causing fluctuations in the Landau distribution (σ_{Landau}) and of the electronic noise (σ_{elec}), which is dominated by two effects: jitter (σ_{jitter}) and time walk ($\sigma_{\text{time walk}}$). While the Landau term can be reduced by using thin sensors, both terms of the electronic noise depend inversely on the signal slope dV/dt:

$$\sigma_{jitter} = \frac{N}{(dV/dt)} \simeq \frac{t_{rise}}{(S/N)}, \quad \sigma_{\text{time walk}} = \left|\frac{V_{th}}{\frac{S}{t_{rise}}}\right|_{RMS} \propto \left|\frac{N}{\frac{dV}{dt}}\right|_{RMS} \tag{2}$$

In this equation, N is the electronic noise, t_{rise} the rise time for the signal, S the signal amplitude and V_{th} the voltage used as threshold to determine the time of arrival. An additional term in the time resolution of the final detector depends on the size of the time-to-digital converter (TDC) bin (σ_{TDC}) [1]. So the final resolution of the sensor, σ_{LGAD} can be seen as:

$$\sigma^2_{\text{LGAD}} = \sigma^2_{\text{Landau}} + \sigma^2_{\text{jitter}} + \sigma^2_{\text{time walk}} + \sigma^2_{\text{TDC}} \tag{3}$$

2 Experimental Framework

2.1 High Luminosity LHC (HL-LHC):

The High Luminosity LHC (HL-LHC) is the Phase II upgrade of the LHC that aims to provide instantaneous luminosity a factor of 10 higher than the LHC design value. At the same time, it seeks to increase the potential for discoveries by expanding the data sample of the experiments [3].

The HL-LHC peak luminosity will reach $5 - 7.5 \times 10^{34} cm^{-2} s^{-1}$ and will achieve an integrated luminosity of $250 fb^{-1}$ per year or more of $3000 fb^{-1}$ in the whole operation period. Its operation is planned to begin in 2028 and run for at least 12 years. All LHC detectors, including ATLAS, have to cope with this upgrade, improving their radiation resistance and improving the ability to process data at much higher speeds. For these reasons, several ATLAS subdetector systems are undergoing significant improvements during the Phase II upgrade [3]. In figure 2 you can see a diagram of the HL-LHC showing its different stages throughout the years of its execution.

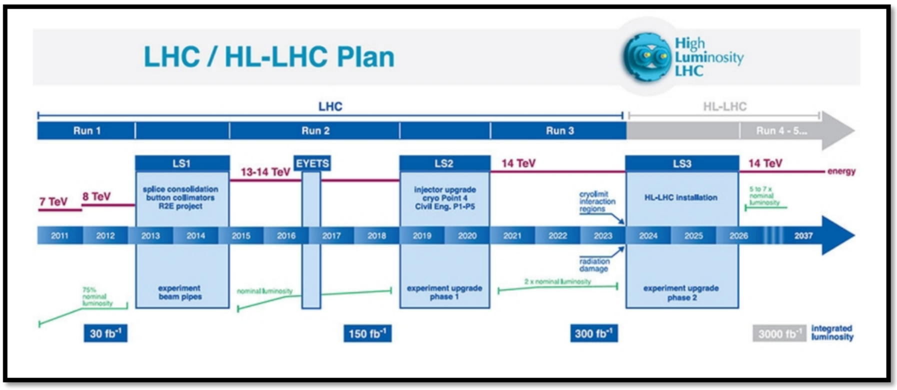

Figure 2: HL-LHC upgrade Plan

The downside of the high luminosity is that with the interesting high-energy collisions (hard-scatter) associated with the primary vertices, soft collisions also occur, i.e. *Pile up*. The *Pile up* is an abrupt increase in the number of collisions that occur in a set of particles crossing a certain area. This increase is such that hard scattering events are *polluted*, which leads to a worse reconstruction of the objects and an increase in the uncertainties of the experimental measurements [3].

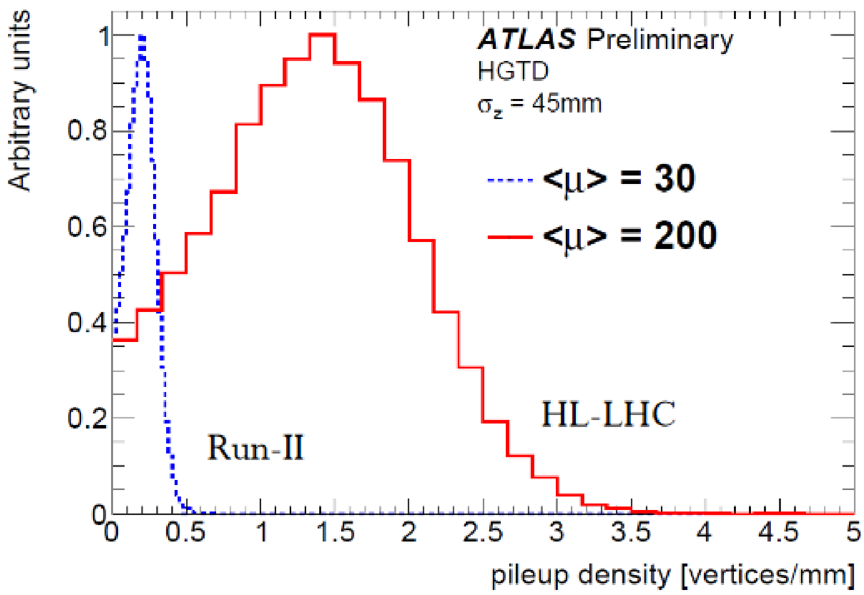

Figure 3: Pile-up differences between Run II (second run of LHC to collide particles and collect data) and HL-LHC. This figure shows that the increase in luminosity produces an increase in the events and consequently in the data obtained [5].

2.2 High Granularity timing detector (HGTD):

The increase of the luminosity at the HL-LHC will rise the number of collisions so high that the follow-up mission will be greatly complicated due to (*Pile up*). *Pile up* occurs when a particle detector's reading includes information from more than one primary beam interaction, or occurs when the detector measures objects that do not come from the primary vertex (*Primary Vertex* or PV), vertex where the *hard scattering* occurs [3]. The primary vertex in this context corresponds to the first vertex produced after the collision of two charged particles, while the series of vertices produced after this (second, third, etc.) are those due to decay processes or interactions other than the main collision. The *Pile up* are those multiple interactions, or interactions that are not of interest.

One of the most difficult challenges in enhancing the LHC's high luminosity is the suppression of detector signals that are caused by additional low-energy collisions between protons. The increase in luminosity will seek to generate collisions that occur at a nominal average of $\mu = 200$ interactions per group or set of particles that crosses a certain area or cross section σ and that has an extension along the axis of the proton halo (perpendicular to σ) of ~ 45 mm. Therefore, ATLAS proposes a high-granularity timing detector (HGTD) [3, 6]. This detector can be seen in figure 4.

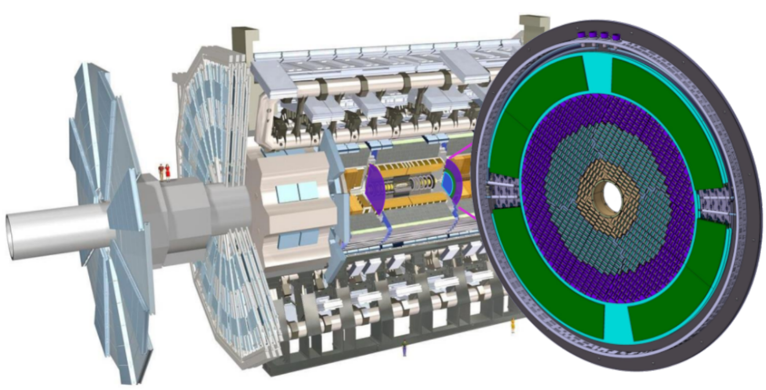

Figure 4: HGTD inside ATLAS [6]

One of the most notable physical and technical characteristics of this detector is that it is composed of two double-sided instrumented layers mounted on two cooling/support discs for each of the two extreme layers of ATLAS. It is also located $z \approx \pm 3.5m$ from the interaction point and has a total radius of 110 mm $< r <$ 1000 mm.

The High Granularity Timing Detector (HGTD) offers a powerful new technique to overcome the *Pile-up* obstacle by by taking advantage of the time spread of interactions, so we can distinguish between interactions that occur very close in space but separated in time. Thus, it is possible to provide a temporal resolution, measurement precision with respect to time, of approximately $30ps$. This will cover the direct region of $2.4 < |\eta| < 4.0$ (equivalent to 120mm $< r <$ 640mm) where the *Pile-up* will be rejected [6].

In this way, as shown in the picture, by using both spatial and temporal information, the tracks can be matched with great certainty to the vertices in the front region of the ATLAS, thus discarding vertices that are not of interest [5]. See figure 5.

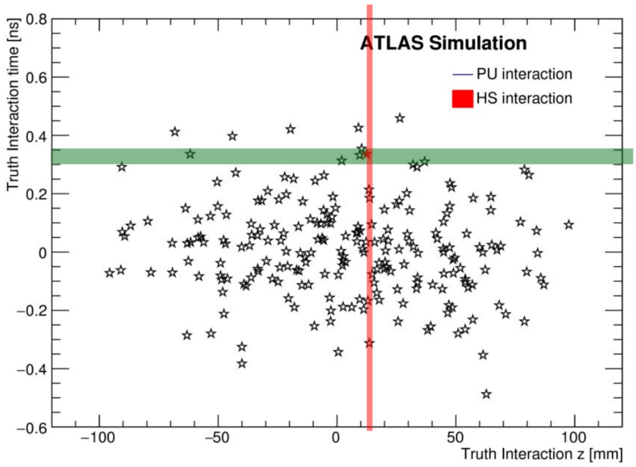

Figure 5: Visualization in the z-t plane of the true interactions in a single bunch of particles crossing the interaction area for simulated events of type $t\bar{t}$ at $\mu = 200$. The red star represents a Hard Scatter event, while the black stars are *Pile-up* interactions. The red line corresponds to the data obtained with ITk and the green line corresponds to the data obtained with HGTD [4].

2.2.1 LGAD Sensors:

Good temporal resolution of the HGTD can be achieved by using **Low Gain Avalanche Detectors** (LGAD), a new semiconductor sensor technology designed for precise timing measurements.

By adding time measurements of the paths followed by particles to the spatial information, HGTD will resolve ambiguities in the path-vertex association. Although a path may appear to spatially align with a particular vertex, differences in path time and selected vertex time can be used to identify and discard paths due to *Pile up* [3]. This is why the sensors choice for the HGTD are the LGAD's: They have a low energy requirement and give a moderate multiplication (gain) on the charge that is collected, which leads to a significant improvement of the signal to noise ratio [3].

Semiconductor detectors are devices used in experimental physics to detect and measure the energy, position and timing of charged particles. The basic operation principle can be explained as follows: a charged particle passing through the detector deposits the energy by ionizing the sensitive material (i.e. creating the free charges: electrons and holes). Under the p-n junction built-in potential the free charge carriers drift to the electrodes, where the induced potential is measured [4].

Now, LGADs are based on implanting a few micrometer thick highly doped p-type layer between the high resistivity p-type bulk and the n^+ implant, which acts as a high-field charge multiplication layer providing moderate gain of about 5–70. These devices are thin pixelated n-on-p silicon sensors with an additional p-type doped layer and whose geometry has been optimized for precision time measurements [1]. As other characteristics, they also have:

- Excellent time resolution < 40 (**50**) ps pre-irradiation (**after-irradiation**).
- Expected charged collected > 15 (**4**) fC pre-irradiation (**after-irradiation**).
- Hit efficiency **> 95%** at the end of lifetime.

In particular, the LGAD sensors can be of Single pad or of nxn array pads. The single sensors has an overall active area of $1.3x1.3mm^2$ (called LGAD). And example of this is shown in the next figure:

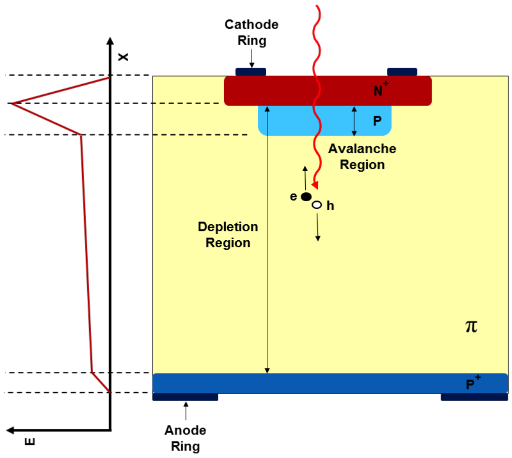

Figure 6: Schematic view of a single pad LGAD diode. On the left hand of the figure, the electric field profile inside the sensor is shown.

3 Methodological Framework

3.1 Devices under test

This work is based on data obtained by 8 LGAD sensors for different design and fluency:

- Two designs, one provided by USTC (University of Science and Technology of China) and the other by IHEP (Institute of High Energies Physics of China).
- Different fluencies: $0 \times 10^{15} neq/cm^2$, $1.5 \times 10^{15} neq/cm^2$, $2.5 \times 10^{15} neq/cm^2$.

The list of the 8 LGAD sensors can be found in the following table:

Table of used Sensors		
Name of the Sensor	**Fluence** (neq/cm^2)	
USTC W7P50	0	Not Irradiated Sensor
IHEP W10P51	0	Not Irradiated Sensor
IHEP W16p43	0	Not Irradiated Sensor
IHEP W16P52	1.5×10^{15}	Irradiated Sensor
USTC W15P49	2.5×10^{15}	Irradiated Sensor
IHEP W16P49	2.5×10^{15}	Irradiated Sensor
USTC W15P1	2.5×10^{15}	Irradiated Sensor
IHEP W10P49	2.5×10^{15}	Irradiated Sensor

Table 1: Sensors under test at SPS test beam campaign in May 2024.

3.2 Beam Test Setup

The results presented in the following sections are obtained from data collected in May 2024, at the H6B beam line of the CERN-SPS (Super Proton Synchrotron) North Area with $E_\pi = 120 GeV$ pions. As it's shown in the figure 7, the test beam experimental setup is composed by:

- ACONITE Telescope for tracking, composed by six MIMOSA planes [7].
- FE14: pixel sensor used for triggering. The pixel pitch size is 0.25 μm $\times$ 0.05 μm.
- MCP (Micro Chamber Plate): a sensor with a very good time resolution (around $10 ps$) and whose main purpose is to work as a time reference for the LGAD sensor.
- Cooling box and chiller are used to keep the sensor at the operational temperature of -30 C.
- 4 Channel High Voltage (HV) power supply provides the power to the sensors under test.
- Data acquisition is performed by MSO58LP Tektronix oscilloscope.

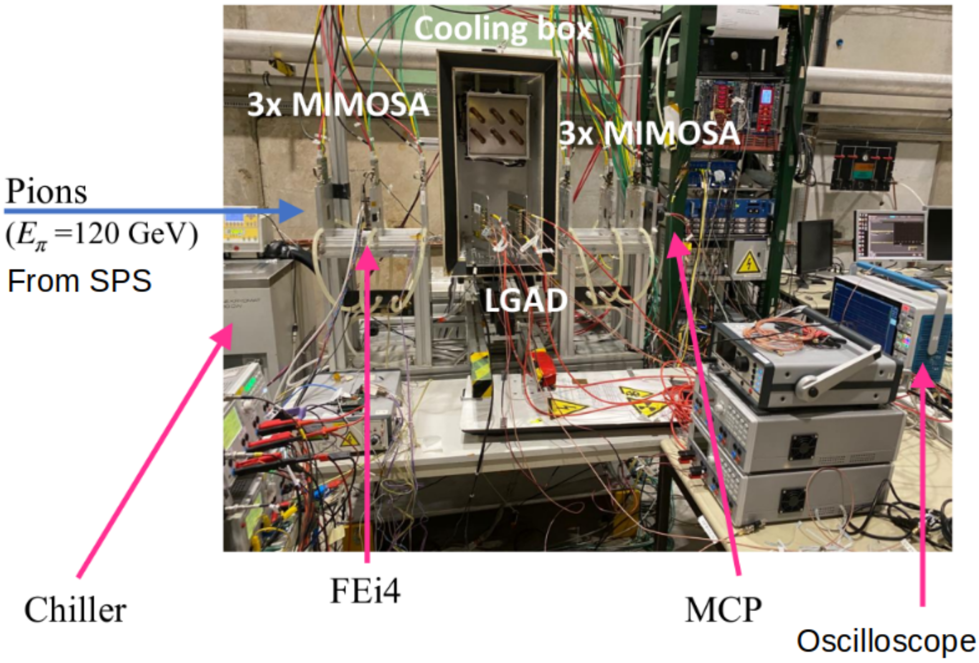

Figure 7: Test-Beam SetUp at CERN

The project has the following objectives:

3.3 Objectives

- Measurement of the time resolution as a function of the HV.
- Measurement of the collected charge as a function of the HV.

4 Analysis and Results

The following sections correspond to the characterization of the 8 sensors its time resolution (σ_{Sensor}), the collected charge as a function of the High Voltage. This analysis was done by using of C++ and ROOT. The codes (in C++) used to produce the plots shown in the next section can be found in: `https://github.com/AdrianJVR/HGTD-Test-Beam-Analysis`

4.1 Efficiency 2D Plots

In order to reduce the contribution of noise, only events that pass through the center of the sensor are used for analysis. The position of the sensor in the local variables (x, y) is obtained looking at 2D efficiency plots produced requiring a collected charge greater than 4 fC is collected by the sensors. The efficiency is defined as:

$$\varepsilon = \frac{\text{Number of events with } Q > 4 \text{ fC}}{\text{Total number of events}} \tag{4}$$

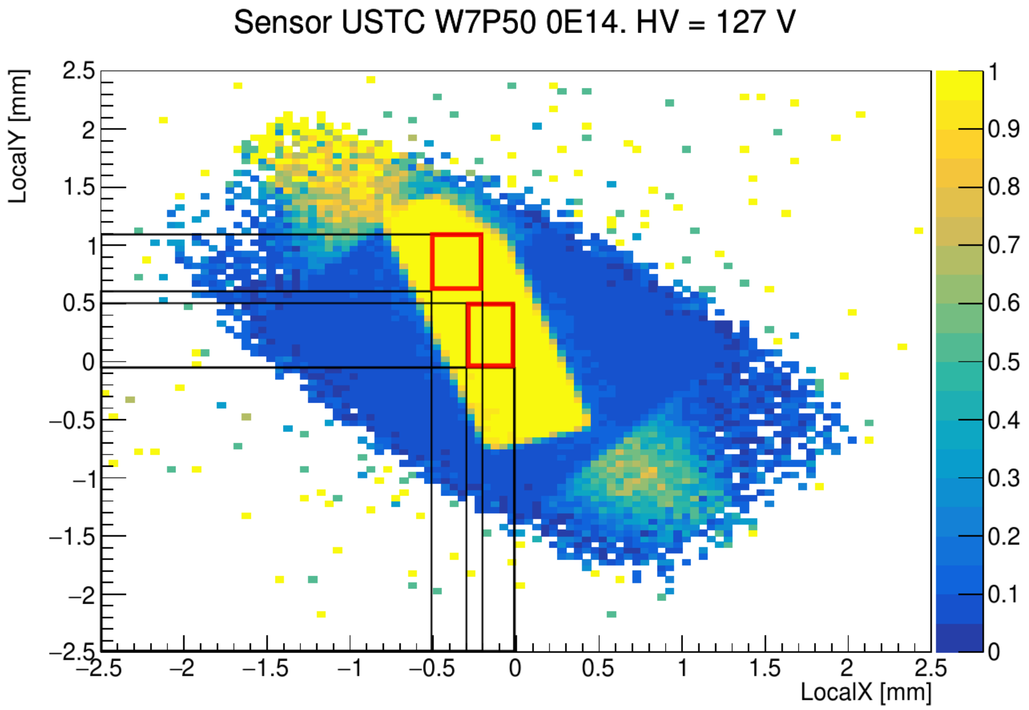

Figure 8: 2D efficiency plot of Sensor USTC W7P50 0E14 for a collected charge $> 4fC$. Events are selected according to geometrical cuts identified by the red rectangles.

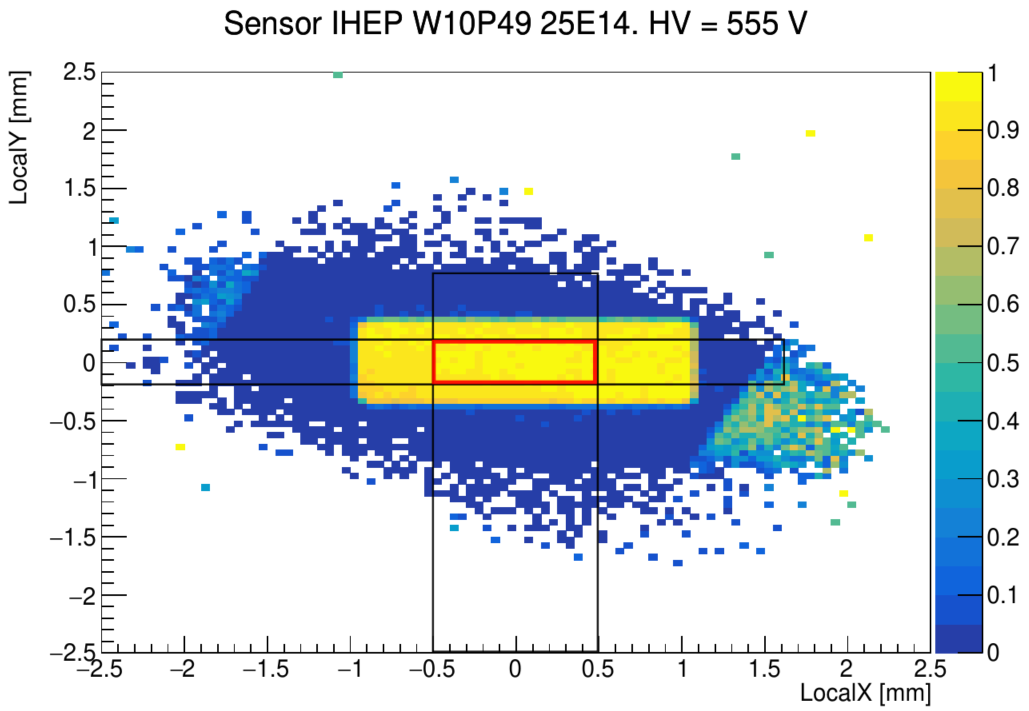

Figure 9: 2D efficiency plot of Sensor IHEP W10P49 25E14 for a collected charge $> 4fC$. Events are selected according to geometrical cuts identified by the red rectangles.

For other sensor, see appendix B. In particular, for plots in figure 8 and 9 the cuts on LocalX and LocalY variables were:

For Sensor USTC W7P50 0E14:

$$-0.3 \text{ mm} < \text{ LocalX } < 0.0 \text{ mm and } -0.05 \text{ mm} < \text{ LocalY } < 0.5 \text{ mm};$$
$$-0.5 \text{ mm} < \text{ LocalX } < -0.2 \text{ mm and } 0.6 \text{ mm} < \text{ LocalY } < 1.1 \text{ mm}$$

For Sensor IHEP W10P49 25E14:

$$-0.5 \text{ mm} < \text{ LocalX } < 0.5 \text{ mm and } -0.2 \text{ mm} < \text{ LocalY } < 0.2 \text{ mm}$$

This same method was applied for all of the sensors, and the obtained geometrical requirements are shown in the following table.

LocalX and LocalY variables cuts for every LGAD Sensor	
Name of the Sensor	**LocalX and LocalY cuts**
USTC W7P50 0E14	-0.3 mm $<$ LocalX < 0.0 mm and -0.05 mm $<$ LocalY < 0.5 mm; -0.5 mm $<$ LocalX < -0.2 mm and 0.6 mm $<$ LocalY < 1.1 mm
IHEP W10P51 0E14	-0.5 mm $<$ LocalX < 0.5 mm and -0.2 mm $<$ LocalY < 0.2 mm
IHEP W16p43 0E14	-1.1 mm $<$ LocalX < -0.75 mm and -0.45 mm $<$ LocalY < 0.2 mm; -0.7 mm $<$ LocalX < -0.3 mm and -0.8 mm $<$ LocalY < -0.45 mm
IHEP W16P52 15E14	-0.4 mm $<$ LocalX < 0.6 mm and -0.15 mm $<$ LocalY < 0.2 mm
USTC W15P49 25E14	0.8 mm $<$ LocalX < 1.2 mm and 1.3 mm $<$ LocalY < 1.6 mm; 0.9 mm $<$ LocalX < 1.3 mm and 0.6 mm $<$ LocalY < 1.2 mm
IHEP W16P49 25E14	-0.5 mm $<$ LocalX < 0.5 mm and -0.2 mm $<$ LocalY < 0.2 mm
USTC W15P1 25E14	-0.55 mm $<$ LocalX < -0.25 mm and 0.0 mm $<$ LocalY < 0.3 mm; -0.35 mm $<$ LocalX < -0.1 mm and -0.4 mm $<$ LocalY < 0.0 mm
IHEP W10P49 25E14	-0.5 mm $<$ LocalX < 0.5 mm and -0.2 mm $<$ LocalY < 0.2 mm

Table 2: Cuts in the LocalX and LocalY variables for the 8 used LGAD sensors in their centers

To consider possible effects of the sensor borders, other LocalX and LocalY cuts were applied such as the following picture shows:

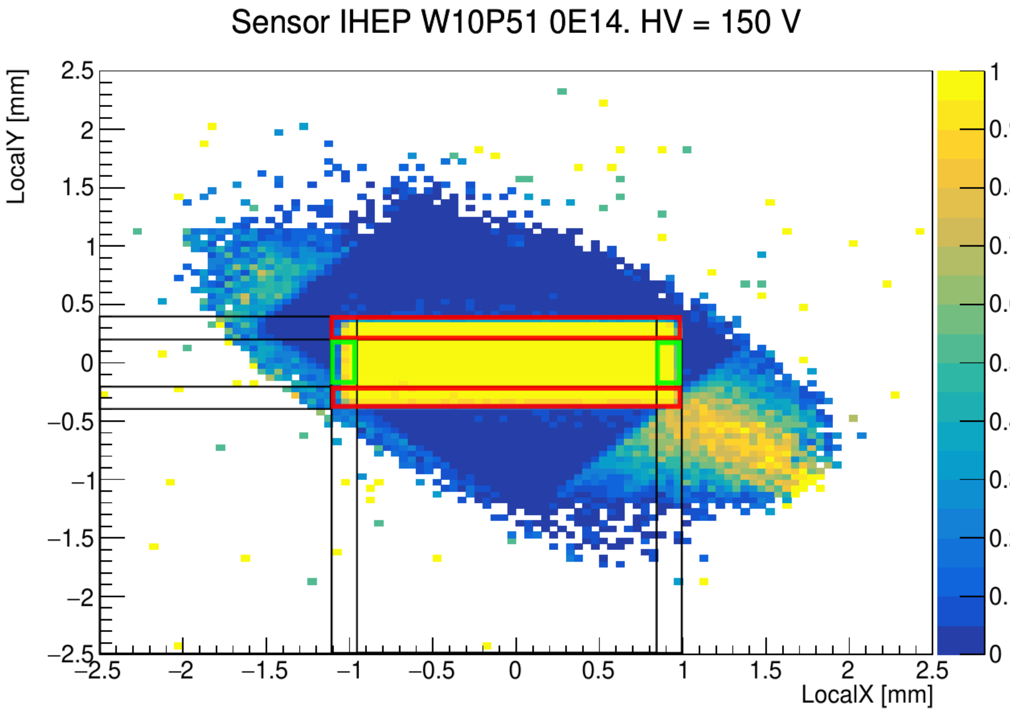

Figure 10: 2D efficiency plot of Sensor IHEP W10P51 0E14 for a collected charge $> 4fC$. Events are selected according to geometrical cuts identified by the red rectangles.

For this plot, the cuts on LocalX and LocalY variables were:

For Sensor IHEP W10P51 0E14:

$$-1.1 \text{ mm} < \text{ LocalX } < 1.0 \text{ mm and } -0.37 \text{ mm} < \text{ LocalY } < -0.2 \text{ mm};$$
$$-1.1 \text{ mm} < \text{ LocalX } < 1.0 \text{ mm and } 0.2 \text{ mm} < \text{ LocalY } < 0.4 \text{ mm};$$
$$-1.1 \text{ mm} < \text{ LocalX } < 0.96 \text{ mm and } -0.2 \text{ mm} < \text{ LocalY } < 0.2 \text{ mm};$$
$$0.85 \text{ mm} < \text{ LocalX } < 1.0 \text{ mm and } -0.2 \text{ mm} < \text{ LocalY } < 0.2 \text{ mm};$$

4.2 Time Resolution

In order to characterize the sensor time resolution, the difference between the Time Of Arrival (TOA) for the MCP and each sensor was used. TOA is defined using CFD (Constant Fraction Discriminator). CFD defines the TOA as the time where the signal reaches the 50% of its total Amplitude.

The difference between TOA is distributed as a Gaussian distribution with a total resolution equal to:

$$\sigma^2_{\text{Gauss}} = \sigma^2_{\text{Sensor}} + \sigma^2_{\text{MCP}} \tag{5}$$

where σ_{MCP} is the MCP resolution which has a measured value $\sigma_{\text{MCP}} = 10$ps. The total resolution is obtained by a Gaussian fit. σ_{Sensor} is extracted after the fit for each HV bias considering σ_{MCP} as a constant value.

As in the previous section, the ΔT distribution (TOA difference between Sensor and MCP) plots for an irradiated and not irradiated sensor are showed. Figure 15 to 18 show the sensor resolution (σ_{Sensor}) as a function of High Voltages.

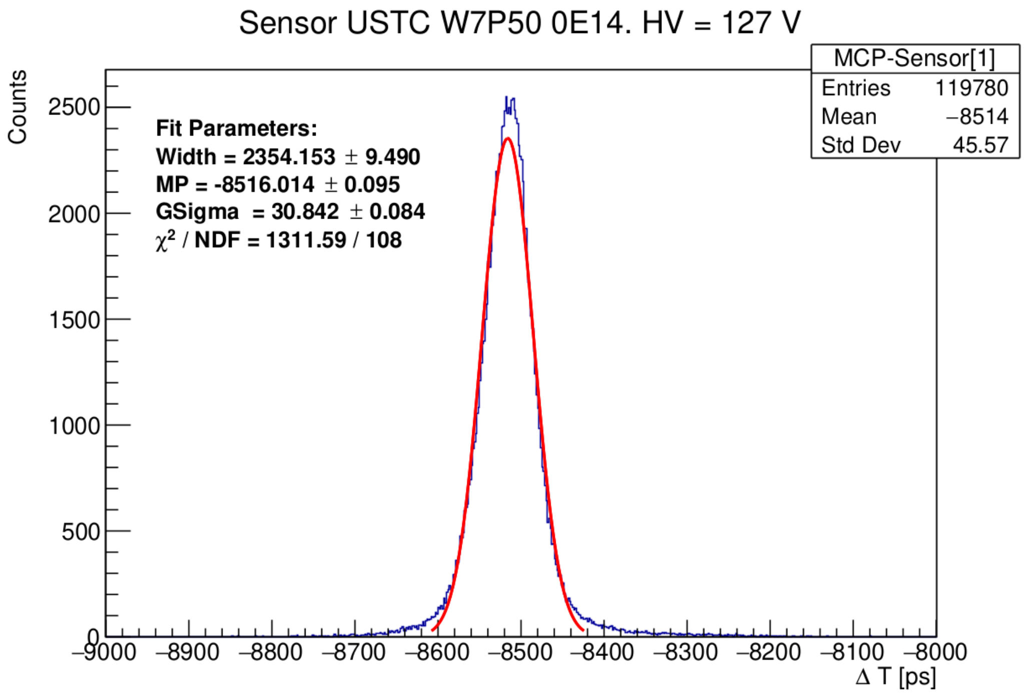

Figure 11: ΔT distribution for Sensor USTC W7P50 0E14 (not irradiated) under a High voltage of 127V. Events are selected according to geometrical cuts at the center of the sensor. For this case, the **Resolution obtained** was $\sigma_{\text{Sensor}} = (29.18 \pm 0.08)ps$ according to equation (5).

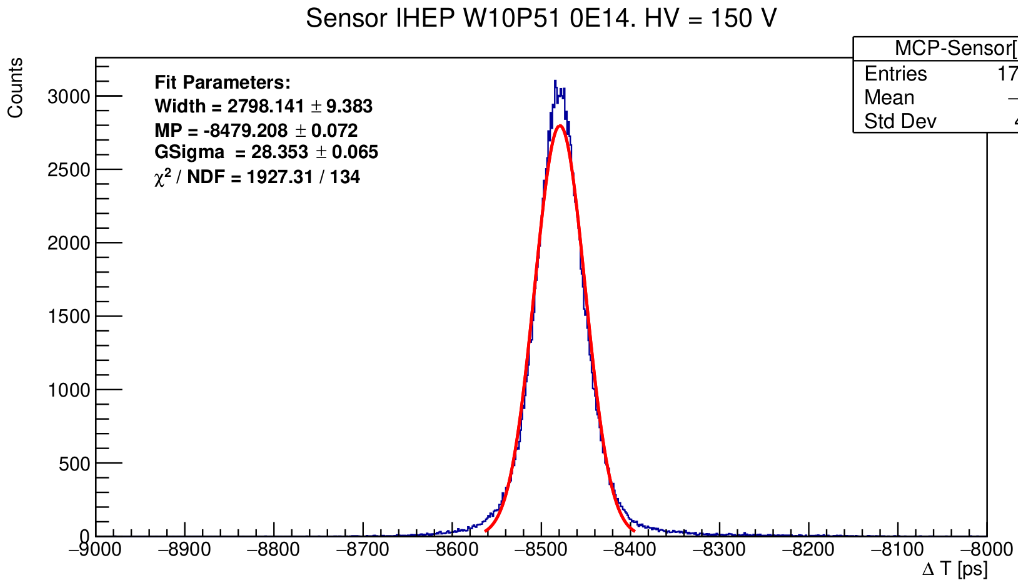

Figure 12: ΔT distribution for Sensor IHEP W10P51 0E14 (not irradiated) under a High voltage of 150V. Events are selected according to geometrical cuts at the center of the sensor. For this case, the **Resolution obtained** was $\sigma_{\text{Sensor}} = (26.54 \pm 0.06)ps$ according to equation (5).

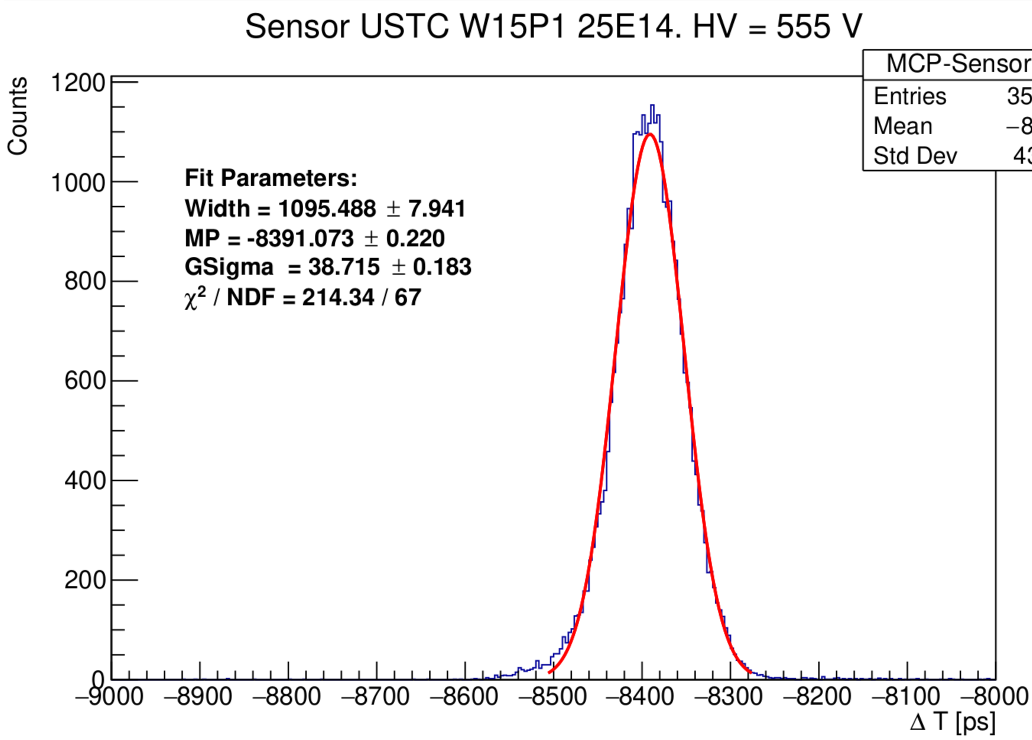

Figure 13: ΔT distribution for Sensor USTC W15P1 25E14 (irradiated) under a High voltage of 555V. Events are selected according to geometrical cuts at the center of the sensor. For this case, the **Resolution obtained** was $\sigma_{\text{Sensor}} = (37.4 \pm 0.2)ps$ according to equation (5).

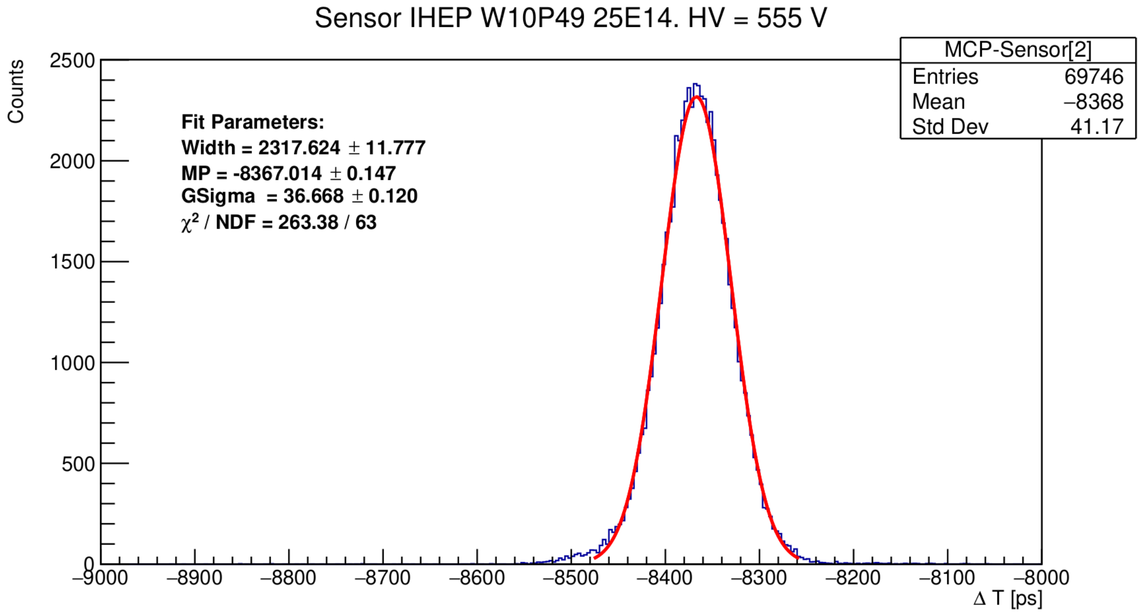

Figure 14: ΔT distribution for Sensor IHEP W10P49 25E14 (irradiated) under a High voltage of 555V. Events are selected according to geometrical cuts at the center of the sensor. For this case, the **Resolution obtained** was $\sigma_{\text{Sensor}} = (35.3 \pm 0.1)ps$ according to equation (5).

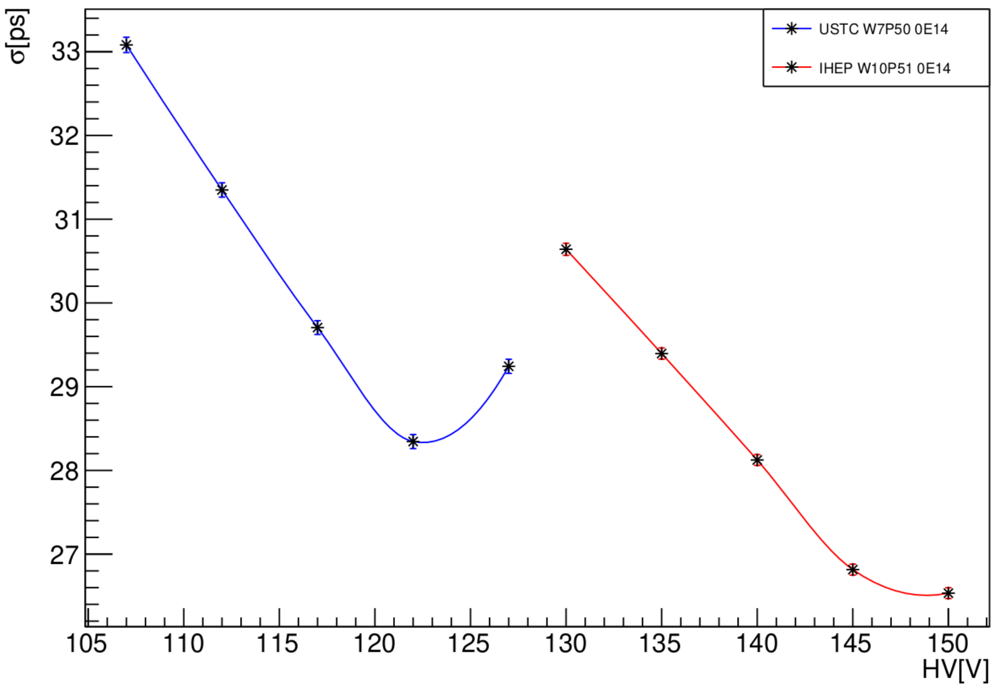

Figure 15: Time resolution of sensor USTC W7P50 0E14 and sensor IHEP W10P51 0E14 as a function of High Voltage (not Irradiated sensors).

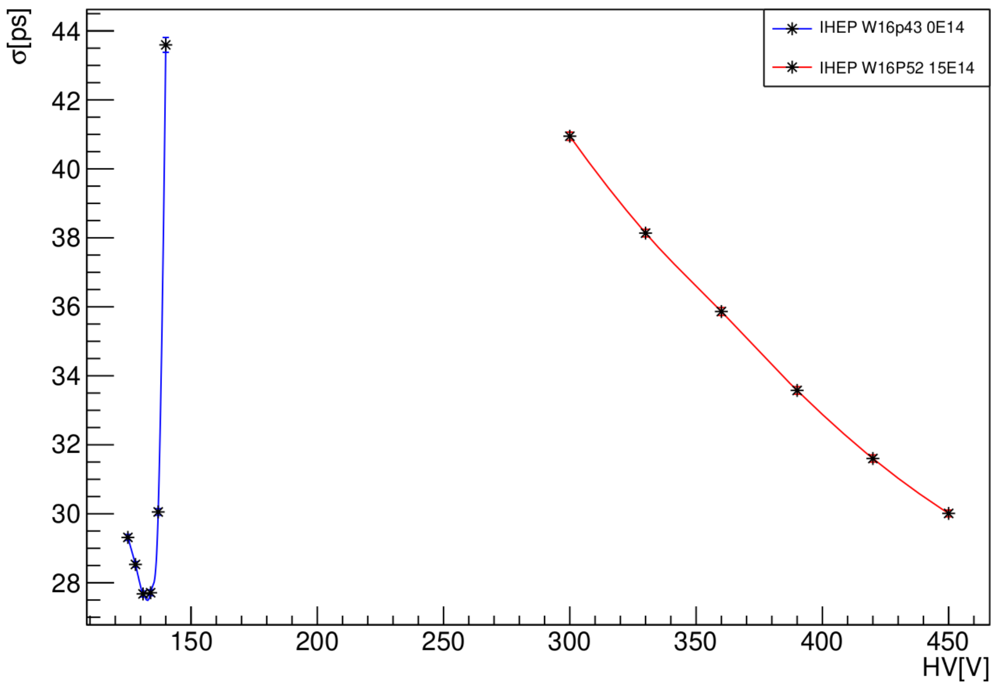

Figure 16: Time resolution of sensor IHEP W16p43 0E14 and sensor IHEP W16P52 15E14 as a function of High Voltage (Not Irradiated and Irradiated sensor).

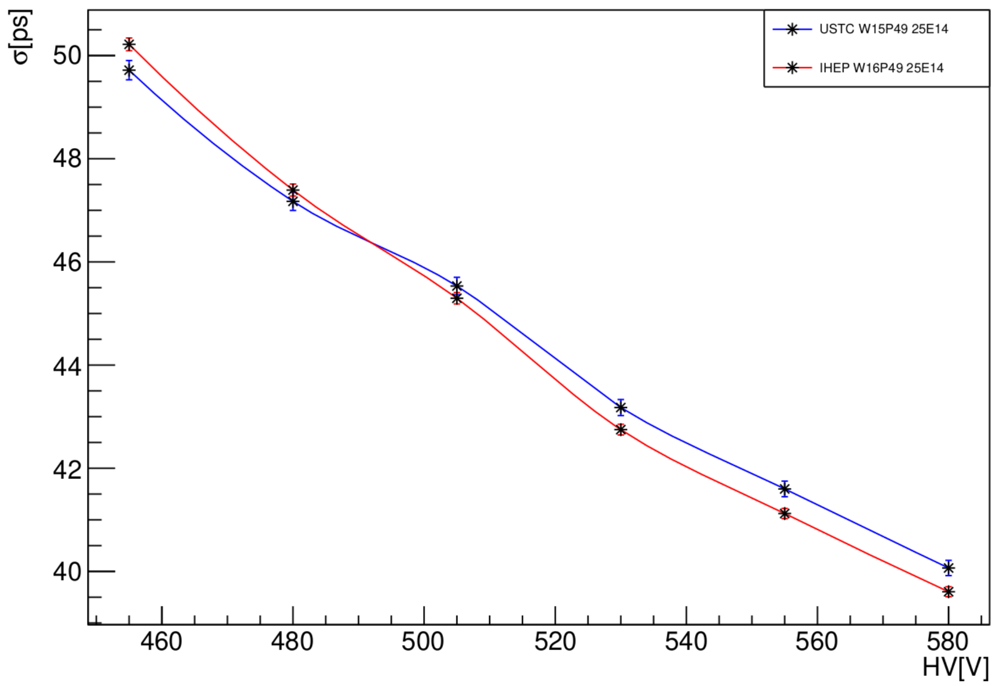

Figure 17: Time resolution of sensor USTC W15P49 25E14 and sensor IHEP W16P49 25E14 as a function of High Voltage (Irradiated sensors).

Comments: The plots show that as the voltage increases, the resolution improves. However, for the case of not irradiated sensors, at some point (breakdown voltage), the Voltage is so high that the resolution gets worse. This can be seen in the picture 15 where breakdown voltage for sensor USTC W7P50 0E14 is around 122V and in picture 16 where the breakdown voltage is around 134V for sensor IHEP W16p43 0E14. The abrupt change in the resolution behaviour happens due to high rate of auto-triggering that happen at voltages after the break-down voltatg value. Except for this single point with high time resolution, the resolution for unirradiated sensor is always lower than 40ps as expected by design requirements.

In the case of the irradiated sensors, it's seen that they need to be under very high values of High voltages to reach a good time resolution due to the radiation damage they have suffered. They all reach the expected design time resolution, lower than 50ps.

as in the case of the not irradiated sensors because

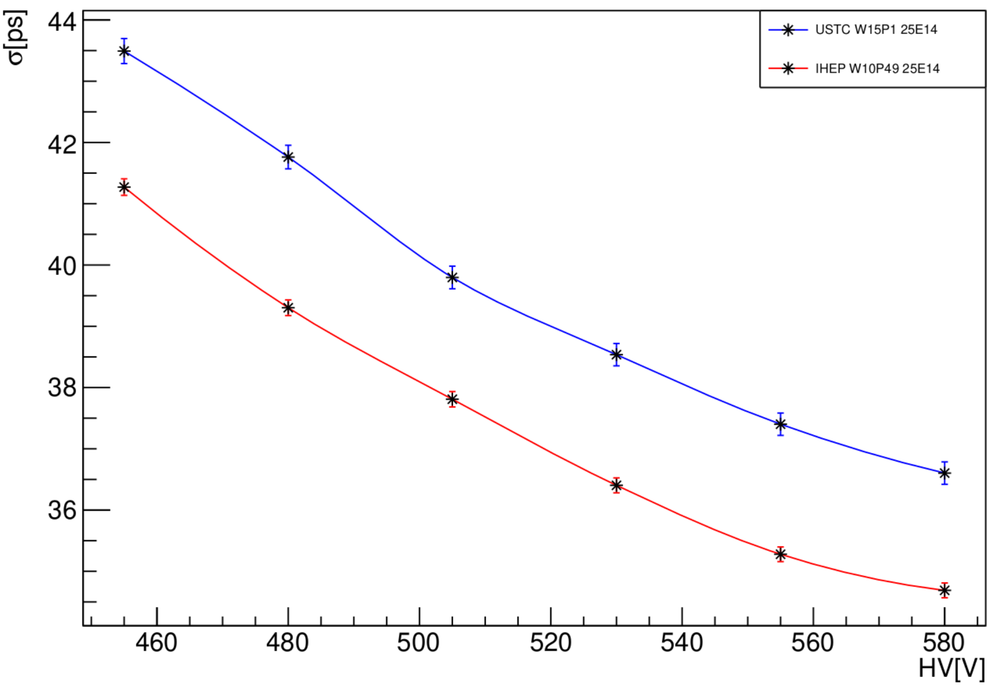

Figure 18: Time esolution of sensor USTC W15P1 25E14 and sensor IHEP W10P49 25E14 as a function of High Voltage (Irradiated sensors).

If instead of a geometrical cut in the center, geometrical selection takes into account the borders and the whole sensor as it's shown in Figure 10, then the following plot can be obtained for sensor IHEP W10P51 0E14:

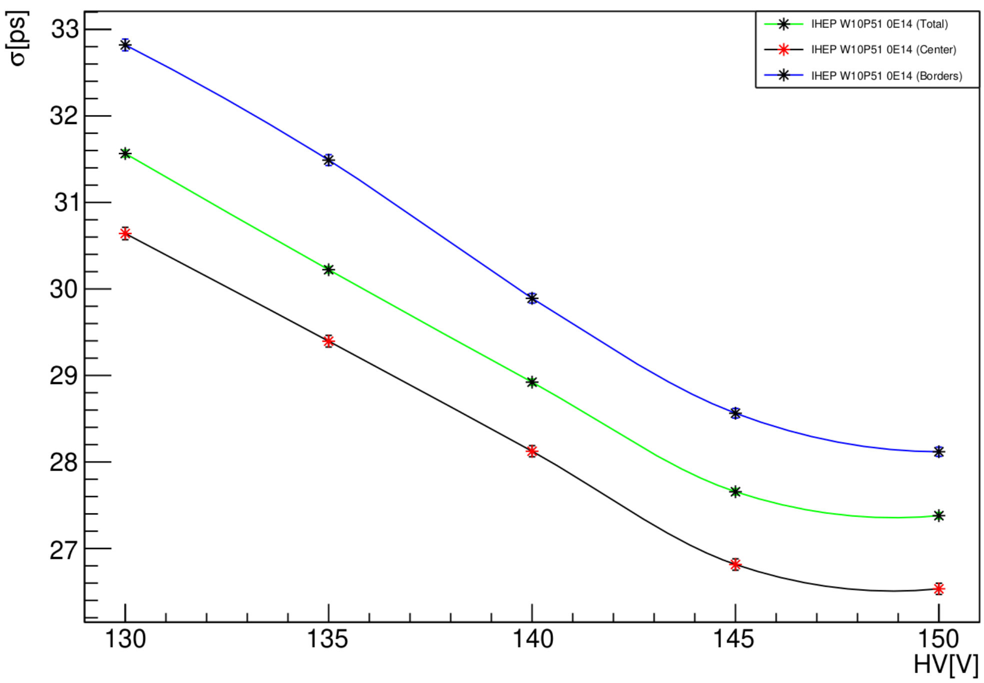

Figure 19: Time resolution of sensor IHEP W10P51 0E14 as a function of High Voltage. For this plot, events are selected in different region of the sensor.

Comments: The difference between the best (center) and the worst (bordes) cases is only 2ps.

4.3 Collected charge Distribution

In this section, the collected charge was studied for all of the sensors according to the geometrical requirements of Section 4.1. The collected charges is defined as the most probable value (MP) obtained from a **Landau-Gaussian convolution fit** on charge distribution. The collected charged is measured performed both for unirradiated and irradiated sensors for different HV values, as for the time resolution measurement

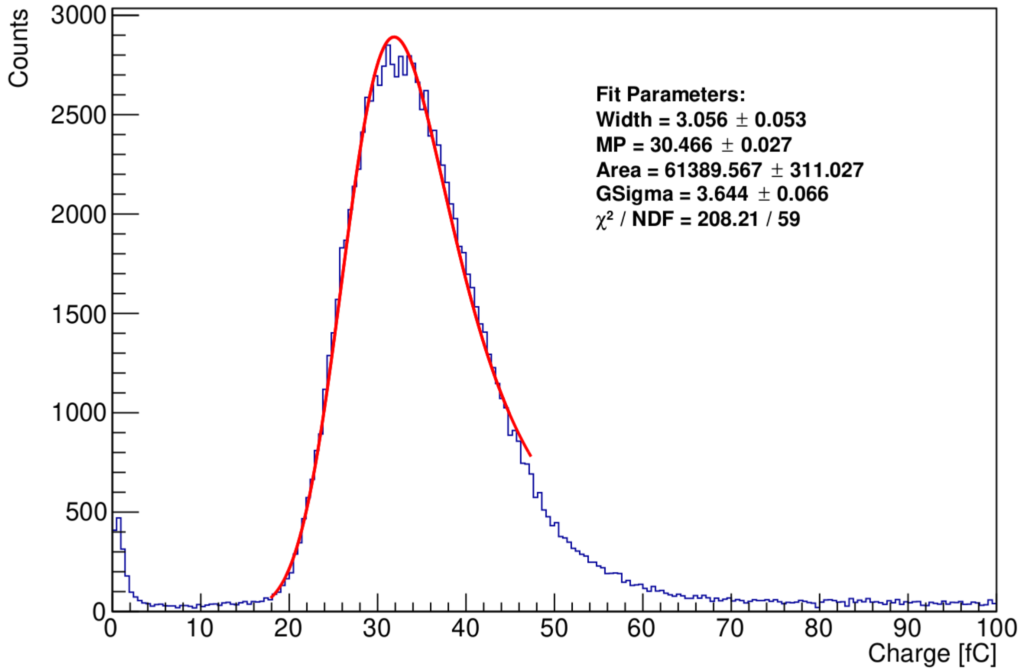

Figure 20: Collected charge distribution for Sensor USTC W7P50 0E14 under a High voltage of 127V. Events are selected according to geometrical cuts at the center of the sensor.

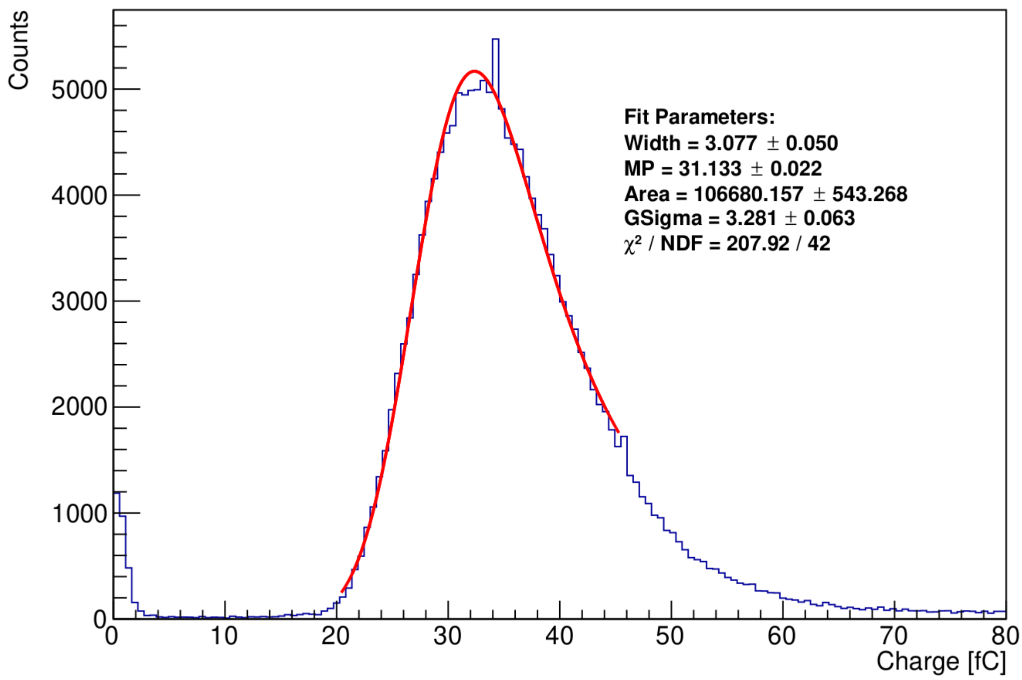

Figure 21: Collected charge distribution for Sensor IHEP W10P51 0E14 under a High voltage of 150V. Events are selected according to geometrical cuts at the center of the sensor.

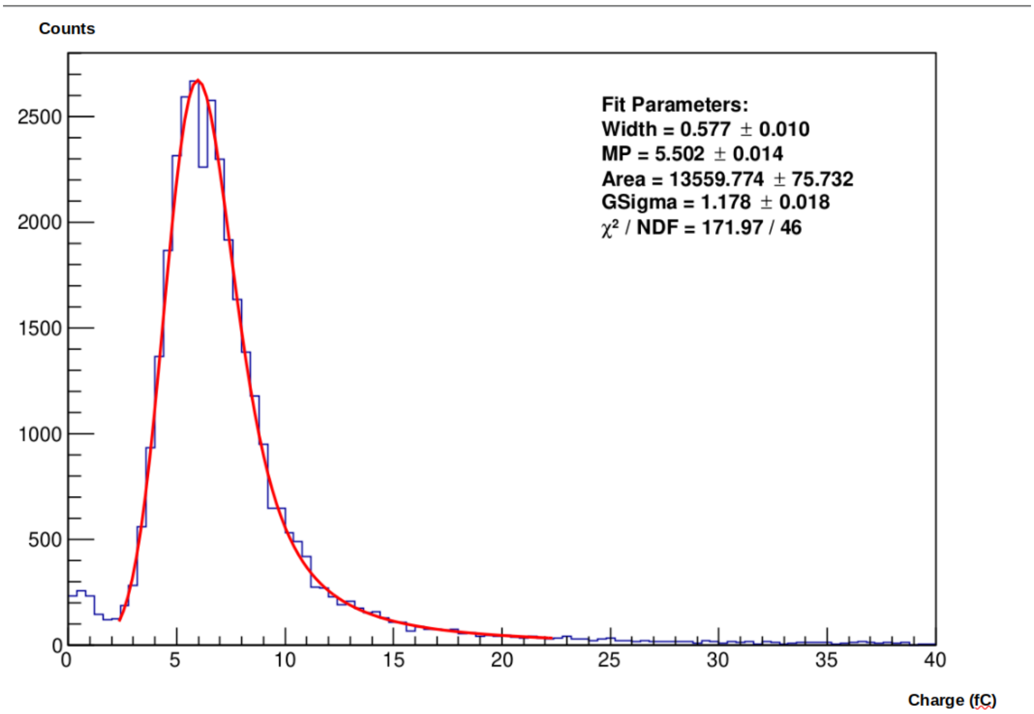

Figure 22: Collected charge distribution for Sensor USTC W15P1 25E14 (irradiated) under a High voltage of 555V. Events are selected according to geometrical cuts at the center of the sensor.

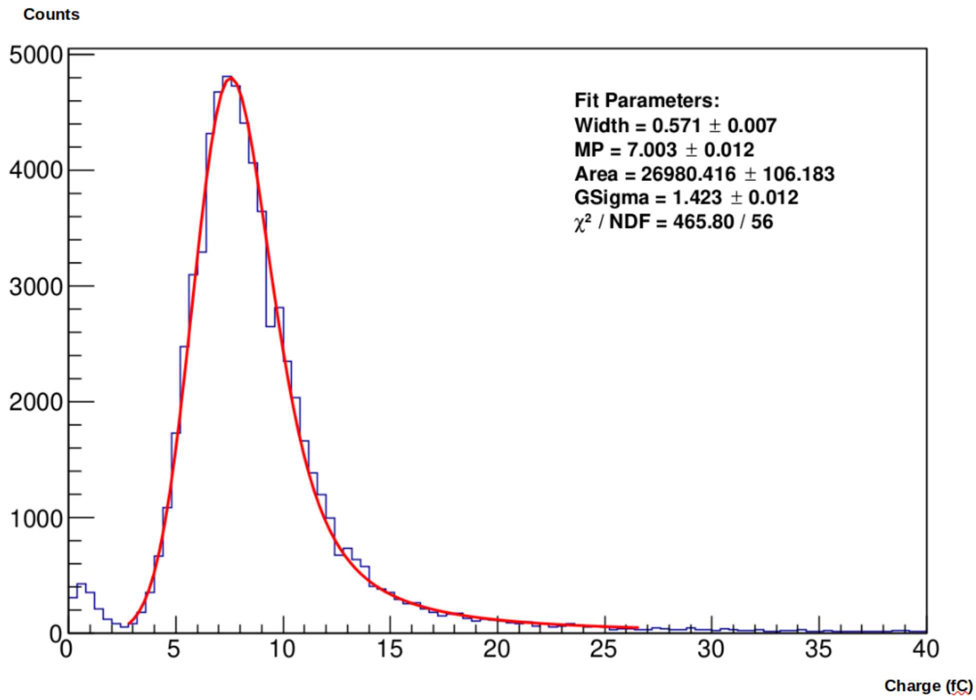

Figure 23: Collected charge distribution for Sensor IHEP W10P49 25E14 (irradiated) under a High voltage of 555V. Events are selected according to geometrical cuts at the center of the sensor.

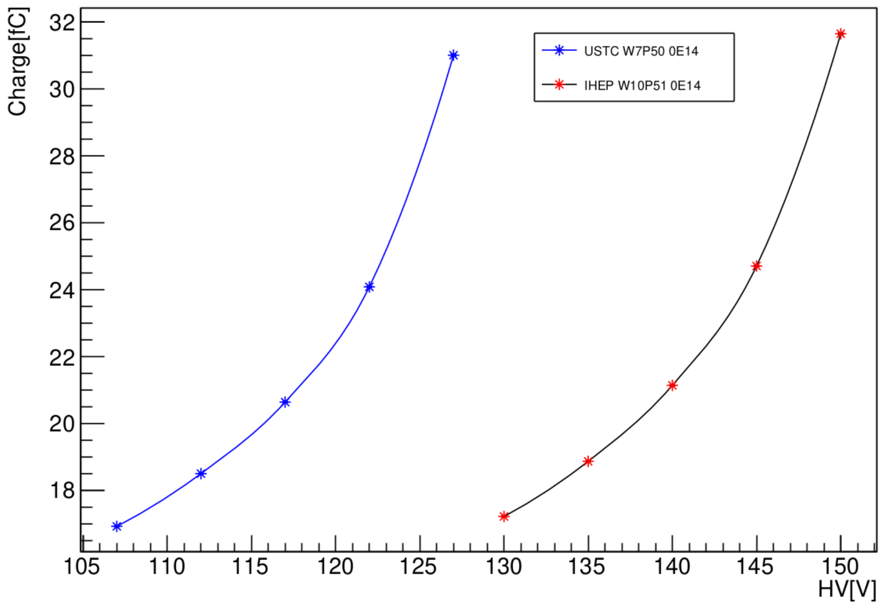

Figure 24: Collected charge most probable value of sensor USTC W7P50 0E14 and sensor IHEP W10P51 0E14 as a function of High Voltage (not Irradiated sensors).

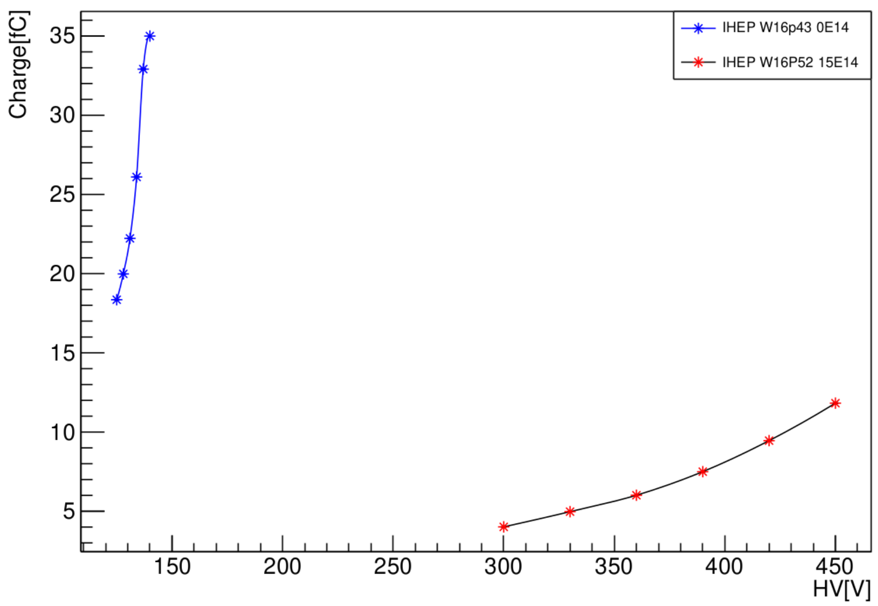

Figure 25: Collected charge most probable value of sensor IHEP W16p43 0E14 and sensor IHEP W16P52 15E14 as a function of High Voltage (Not Irradiated and Irradiated sensor).

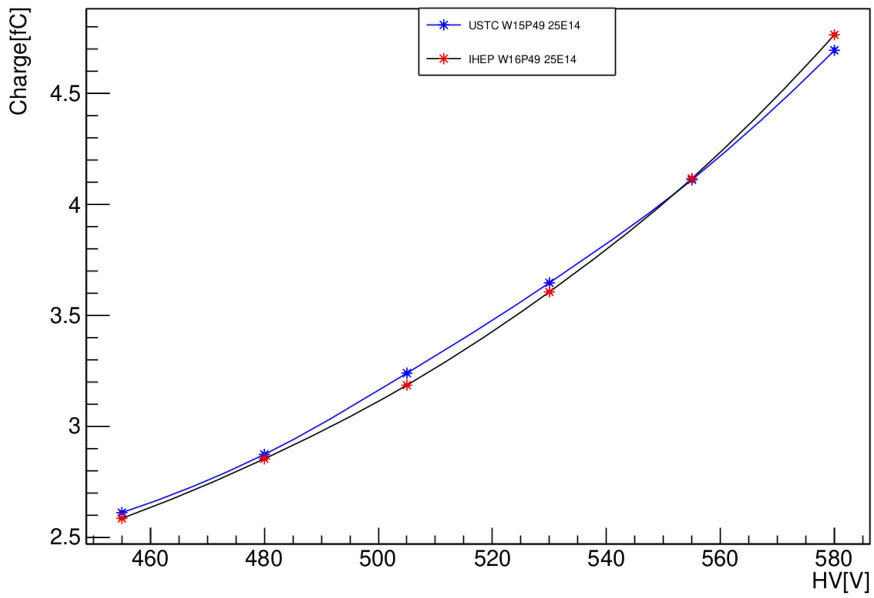

Figure 26: Collected charge most probable value of sensor USTC W15P49 25E14 and sensor IHEP W16P49 25E14 as a function of High Voltage (Irradiated sensors).

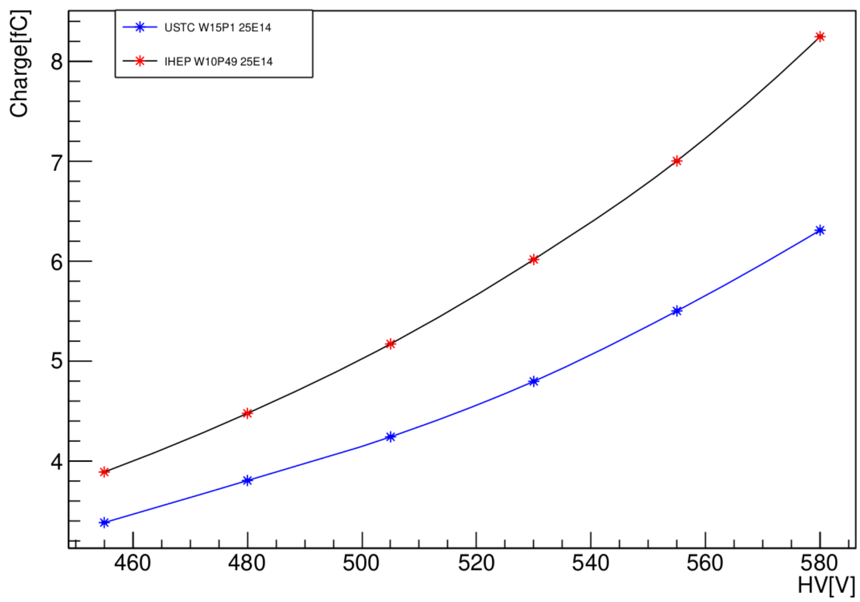

Figure 27: Collected charge most probable value of sensor USTC W15P1 25E14 and sensor IHEP W10P49 25E14 as a function of High Voltage (Irradiated sensors).

Comments: The plots show that as the voltage increase, the collected charge also increases for irradiated and not irradiated sensors.The irradiated and not irradiated sensors can reach the charge threshold expected by HGTD design requirements: higher than 15 fC for unirradiated sensor and 4 fC for irradiated sensors.

5 Conclusions

The measurement of 8 LGAD pre-production sensors for the HGTD ATLAS upgrade project has been performed. The 8 sensors are characterized by different design, and different level of irradiation to which they have been exposed. The sensor performance is characterized in terms of time resolution and collected charge. All the sensors can reach the design requirements for time resolution, < 40 pS and < 50 pS for unirradiated and irradiated sensors respectively, and for collected charge, > 15 fC and > 4 fC for unirradiated and irradiated sensors respectively.

6 References

[1] C. Allaire, J. Benitez, M. Bomben, G. Calderini, M. Carulla, E. Cavallaro, A. Falou, D. Flores, P. Freeman, Z. Galloway, E.L. Gkougkousis, H. Grabas, S. Grinstein, B. Gruey, S. Guindon, A.M. Henriques Correia, S. Hidalgo, A. Kastanas, C. Labitan, D. Lacour, J. Lange, F. Lanni, B. Lenzi, Z. Luce, N. Makovec, G. Marchiori, L. Masetti, A. Merlos, F. McKinney-Martinez, I. Nikolic-Audit, G. Pellegrini, R. Polifka, D. Quirion, A. Rummler, H.F-W. Sadrozinski, A. Seiden, L. Serin, S. Simion, E. Spencer, S. Trincaz-Duvoid, M. Wilder, A. Zatserklyaniy, D. Zerwasa and Y. Zhao. [2018]. *Beam test measurements of Low Gain Avalanche Detector single pads and arrays for the ATLAS High Granularity Timing Detector*. Recovered from: `https://arxiv.org/abs/1804.00622`.

[2] G. Aad *et al.* [ATLAS], JINST **3** (2008), S08003 doi:10.1088/1748-0221/3/08/S08003

[3] M. Alshamsi (2020). *The ATLAS High Granularity Timing Detector*. University Of Sharjah, Sharjah, United Arab Emirates. Recovered from: `https://cds.cern.ch/record/2651090/files/hgtd-2.pdf`.

[4] Riani H. on behalf of the ATLAS HGTD Group (2023). Simulation of the ATLAS High Granularity Timing Detector geometry in the ATLAS framework. University Mohamed First Oujda. Rabat, Morocco.

[5] Allaire C. on behalf of the ATLAS LAr-HGTD group (2018). *A High-Granularity Timing Detector in ATLAS : Performance at the HL-LHC*. Univ. Paris-Sud, CNRS/IN2P3, Universit Paris-Saclay, Orsay, France. ATL-LARG-PROC-2018-003.

[6] V. Raskina, S. Trincaz-Duvoid, T, Beau. (2023). *Research and development of the High-Granularity Timing Detector (HGTD) for the ATLAS Detector as the preparation of the High-Luminosity LHC operation phase.* LPNHE, France. Recovered from: `https://cernbox.cern.ch/s/z2sc5NLgnVpBPOp`

[7] H. Jansen, S. Spannagel, A. Bulgheroni, G. Claus, E. Corrin, D. G. Cussans, J. Dreyling-Eschweiler, D. Eckstein, T. Eichhorn and M. Goffe, *et al.* EPJ Tech. Instrum. **3** (2016) no.1, 7 doi:10.1140/epjti/s40485-016-0033-2 [arXiv:1603.09669 [physics.ins-det]].

Appendix A Maximum Voltage Amplitude (Amax)

The next plots show the maximum voltage amplitude distribution obtained by the sensors for several High Voltage values into consideration.

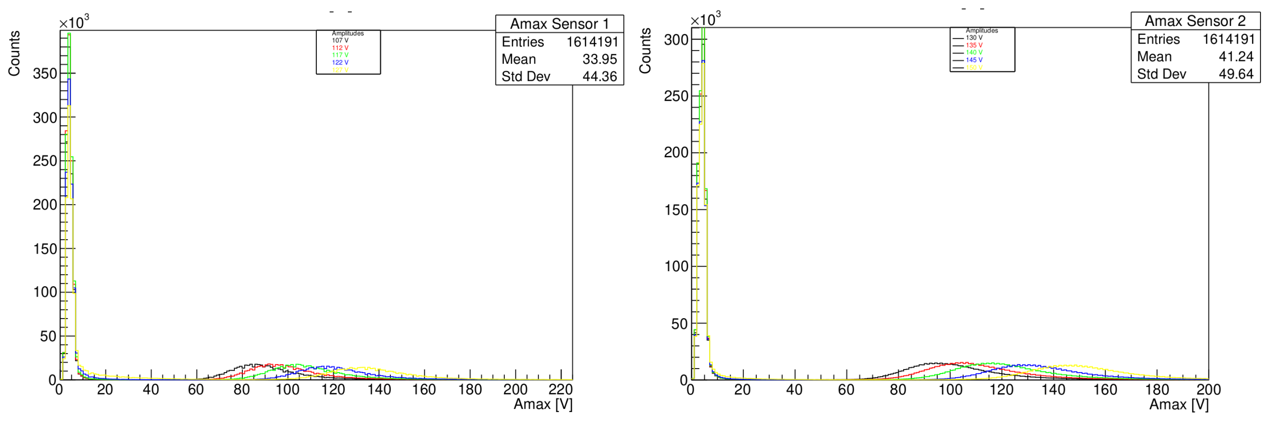

(a) Amax distribution of Sensor USTC W7P50 0E14 for different High Voltage values

(b) Amax distribution of Sensor IHEP W10P51 0E14 for different High Voltage values

Figure 28: Maximum Voltage Amplitude (Amax) of two not Irradiated sensors (USTC W7P50 0E14 and IHEP W10P51 0E14).

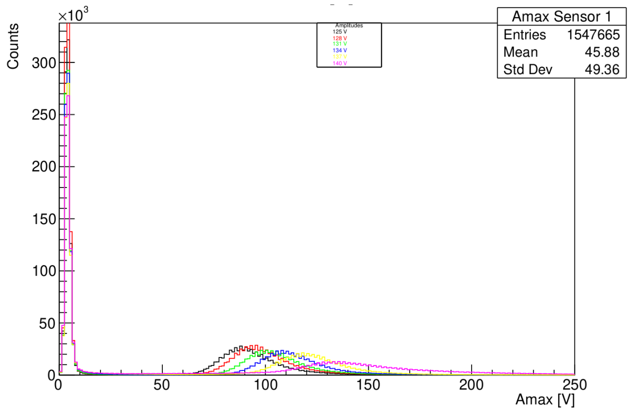

(a) Amax distribution of Sensor IHEP W16p43 0E14 for different High Voltage values

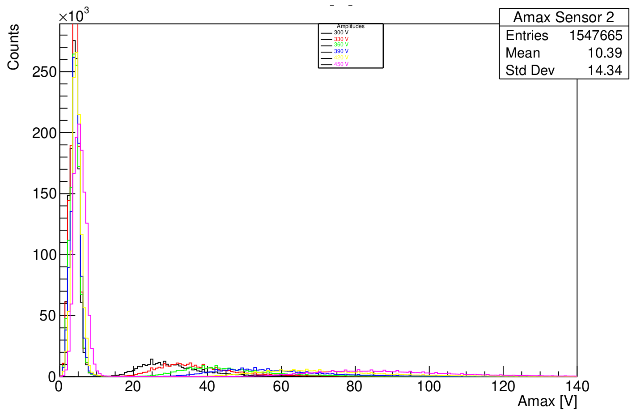

(b) Amax distribution of Sensor IHEP W16P52 15E14 for different High Voltage values

Figure 29: Maximum Voltage Amplitude (Amax) of a not Irradiated and Irradiated sensor (UIHEP W16p43 0E14 and IHEP W16P52 15E14 respectively).

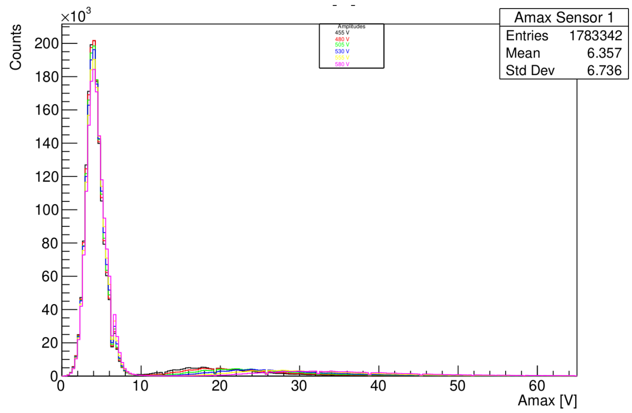

(a) Amax distribution of Sensor USTC W15P49 25E14 for different High Voltage values

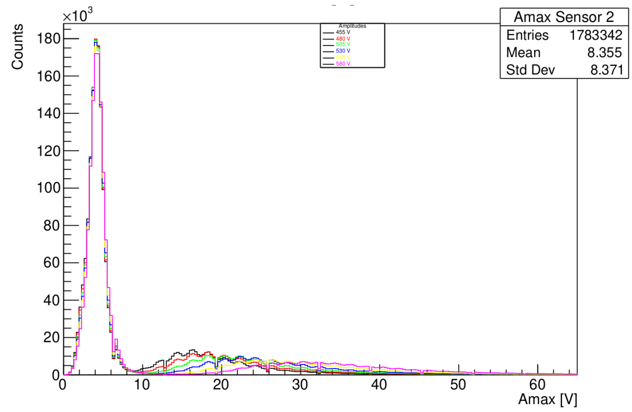

(b) Amax distribution of Sensor IHEP W16P49 25E14 for different High Voltage values

Figure 30: Maximum Voltage Amplitude (Amax) of two Irradiated sensors (USTC W15P49 25E14 and IHEP W16P49 25E14)

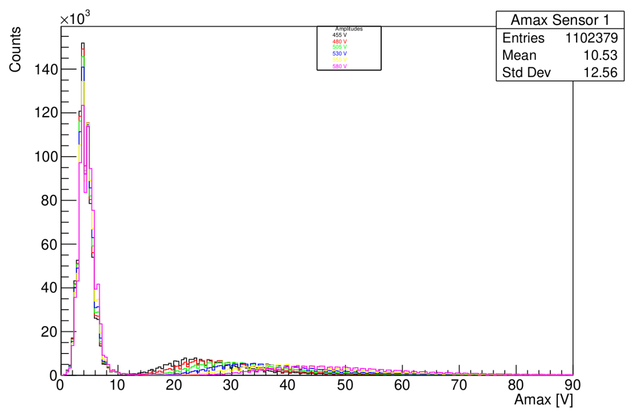

(a) Amax distribution of Sensor USTC W15P1 25E14 for different High Voltage values

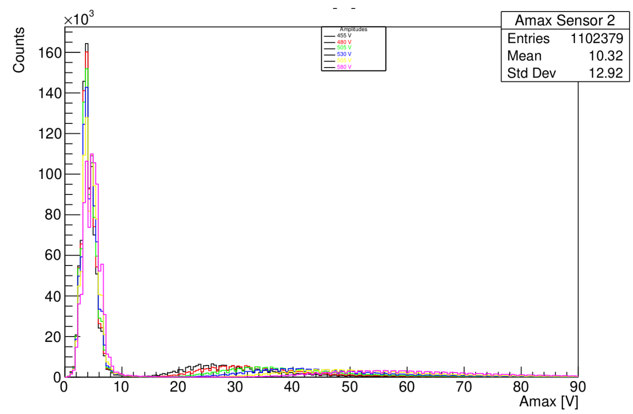

(b) Amax distribution of Sensor IHEP W10P49 25E14 for different High Voltage values

Figure 31: Maximum Voltage Amplitude (Amax) of two Irradiated sensors (USTC W15P1 25E14 and IHEP W10P49 25E14)

Additionally, The next pair of plots shows a comparison between the Amax of the irradiated and not irradiated sensors with a very high difference in the High voltage they experienced:

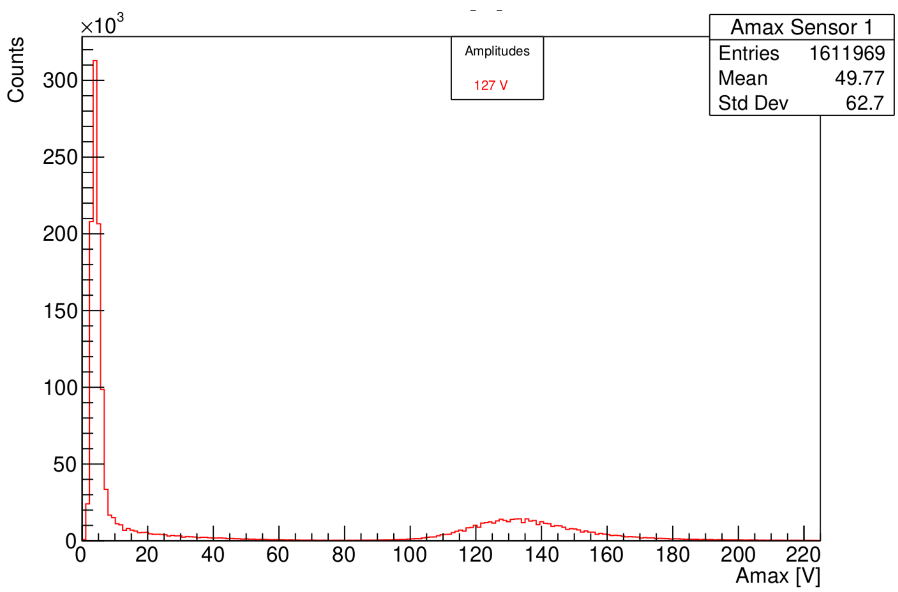

Figure 32: Amax distribution for the sensor USTC W7P50 0E14 under a High Voltage of 127V.

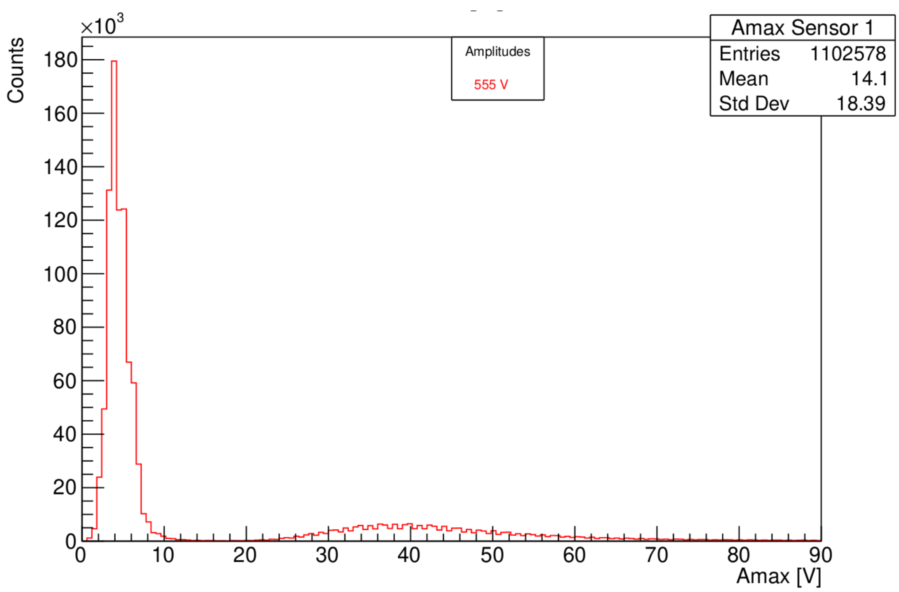

Figure 33: Amax distribution for the sensor USTC W15P1 25E14 under a High Voltage of 555V.

Comments: The plots show that there's always a big contribution in Amax due to noise, so for the highest fluence sensor the cut on Amax cannot separate signal from noise. It's also observed than the higher the radiation damage, the smaller the Amax. At the end, it can be concluded that only the Amax distribution is not enough to make a good characterization of the sensors.

Appendix B Efficiency 2D Plots

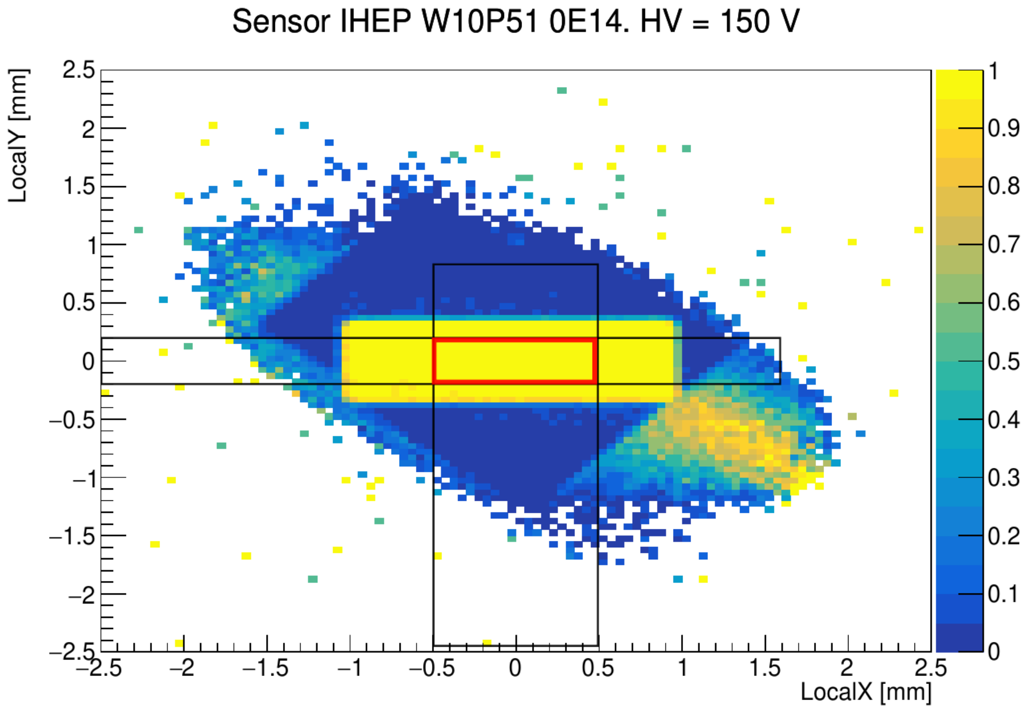

Figure 34: 2D efficiency plot of Sensor IHEP W10P51 0E14 for a collected charge greater than $4fC$. Events are selected according to geometrical cuts identified by the red rectangles.

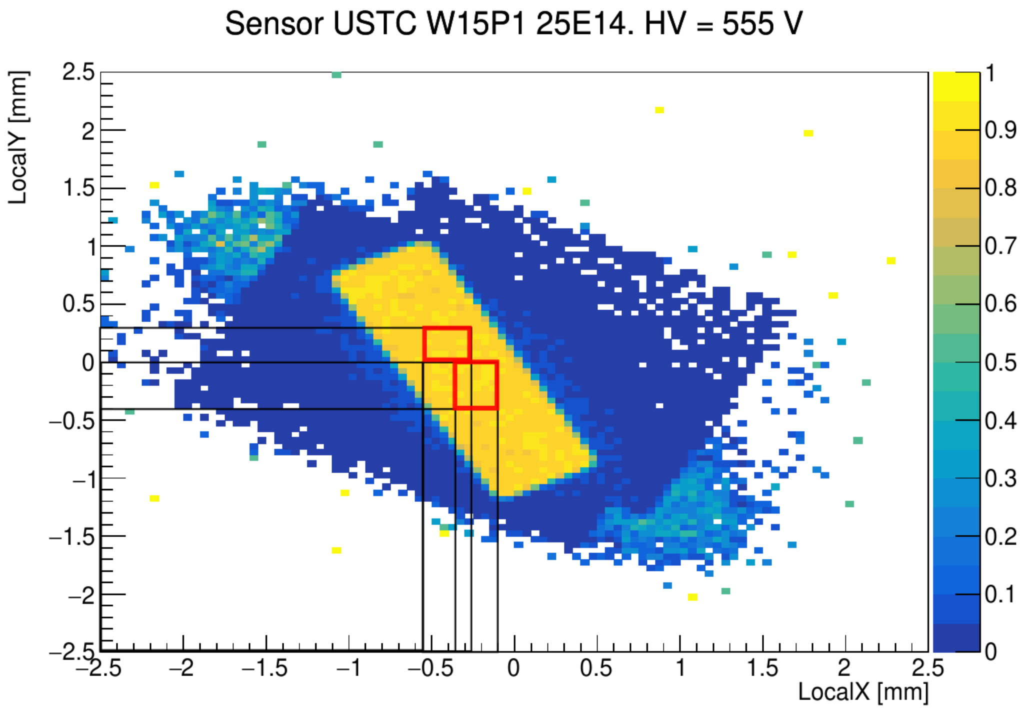

Figure 35: 2D efficiency plot of Sensor USTC W15P1 25E14 for a collected charge greater than of $4fC$. Events are selected according to geometrical cuts identified by the red rectangles.

For this plots, the cuts on LocalX and LocalY variables were:

For Sensor USTC W15P1 25E14:

$$-0.55 \text{ mm} < \text{ LocalX } < -0.25 \text{ mm and } 0.0 \text{ mm} < \text{ LocalY } < 0.3 \text{ mm;}$$
$$-0.35 \text{ mm} < \text{ LocalX } < -0.1 \text{ mm and } -0.4 \text{ mm} < \text{ LocalY } < 0.0 \text{ mm}$$

For Sensor IHEP W10P51 0E14:

$$-0.5 \text{ mm} < \text{ LocalX } < 0.5 \text{ mm and } -0.2 \text{ mm} < \text{ LocalY } < 0.2 \text{ mm}$$

Appendix C Time Resolution

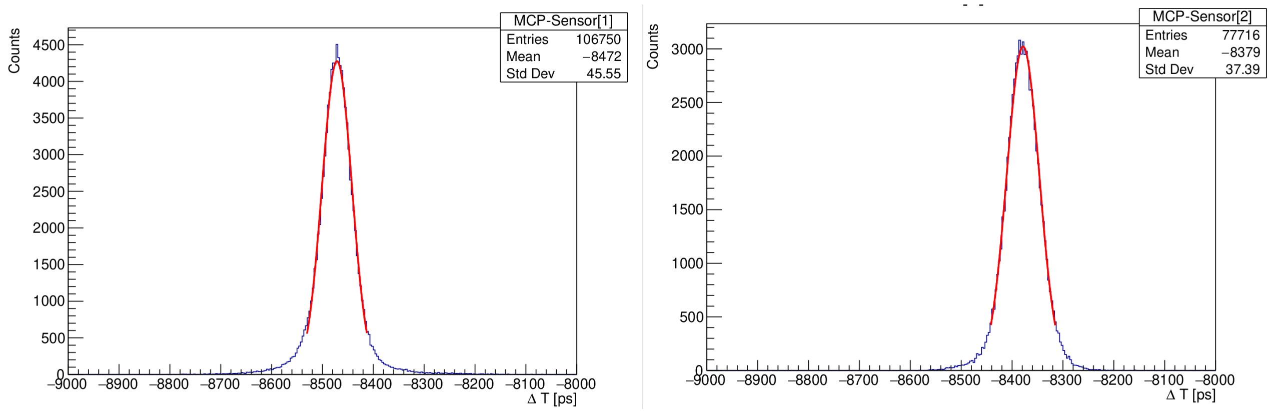

(a) ΔT for Sensor IHEP W16p43 0E14 under a High Voltage of 137V

(b) ΔT for Sensor IHEP W16P52 15E14 under a High voltage of 420V

Figure 36: ΔT distribution for an irradiated and not irradiated sensor.

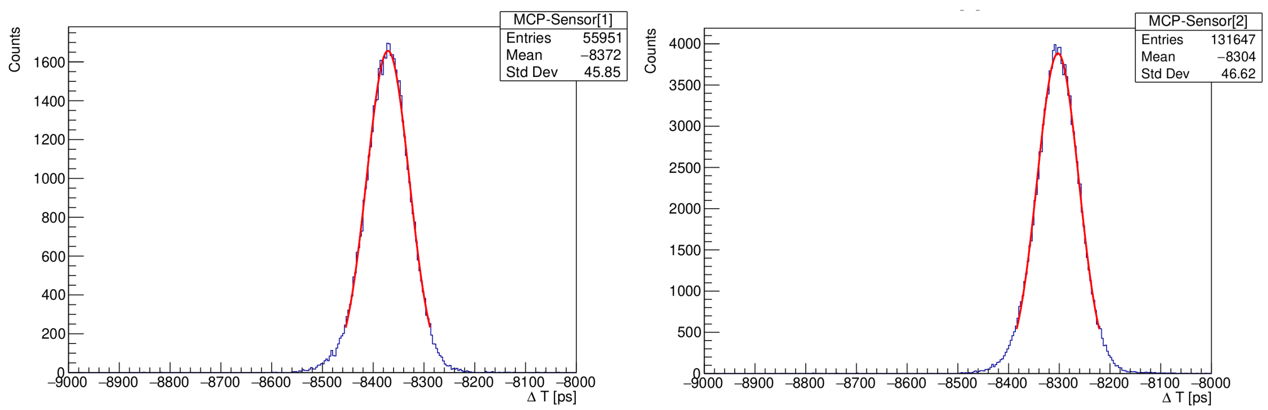

(a) ΔT for Sensor USTC W15P49 25E14 under a High voltage of 555V

(b) ΔT for Sensor IHEP W16P49 25E14 under a High voltage of 555V

Figure 37: ΔT distribution for two irradiated sensors

Appendix D Collected charge Distribution

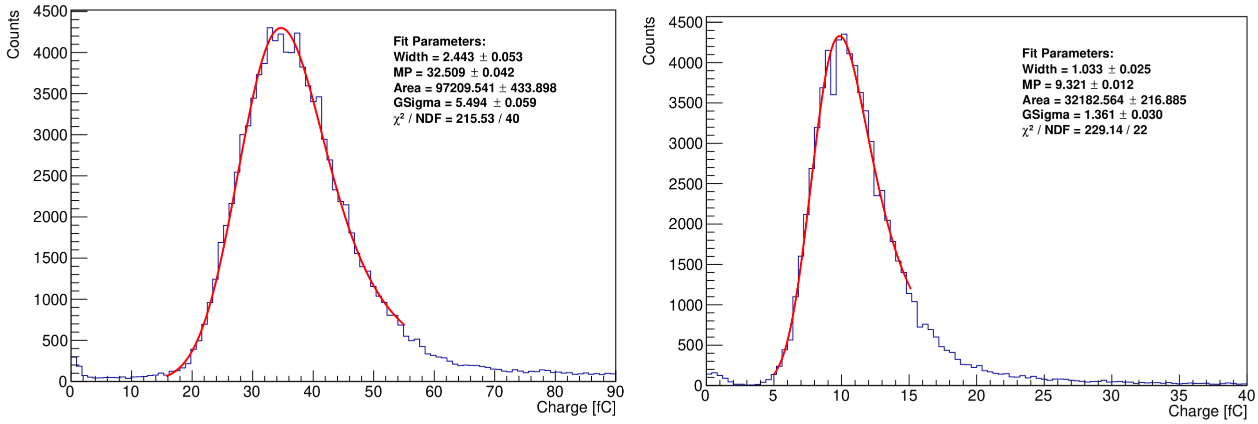

(a) Collected charge distribution for Sensor IHEP W16p43 0E14 under a High Voltage of 137V

(b) Collected charge distribution for Sensor IHEP W16P52 15E14 under a High voltage of 420V

Figure 38: Collected charge distribution for an irradiated and not irradiated sensor.

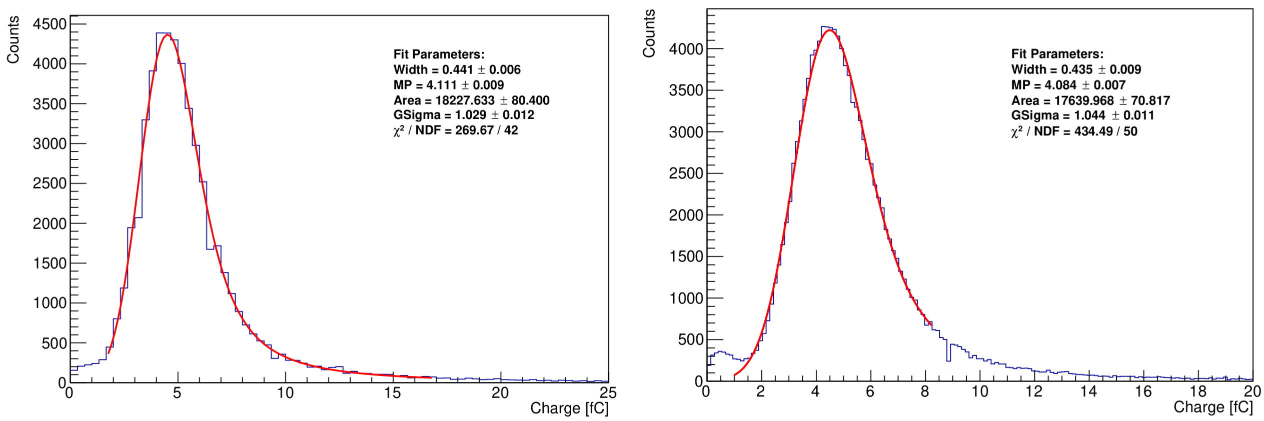

(a) Collected charge distribution for Sensor USTC W15P49 25E14 under a High voltage of 555V

(b) Collected charge distribution for Sensor IHEP W16P49 25E14 under a High voltage of 555V

Figure 39: Collected charge distribution for two irradiated sensors.